The Spine Journal 19 (2019) 2013–2024

Basic Science

Material properties of human lumbar intervertebral discs across strain rates

Nicolas Newell, PhD[a,*], Diagarajen Carpanen, PhD[a], Grigorios Grigoriadis, PhD[a], J. Paige Little, PhD[b,c], Spyros D. Masouros, PhD[a]

[a] *Department of Bioengineering, Imperial College London, London SW7 2AZ, United Kingdom*
[b] *Paediatric Spine Research Group, Queensland University of Technology, Brisbane, Queensland, Australia*
[c] *Mater Health Services Brisbane Ltd, Brisbane, Queensland, Australia*

Received 2 March 2019; revised 16 July 2019; accepted 17 July 2019

Abstract

BACKGROUND CONTEXT: The use of finite element (FE) methods to study the biomechanics of the intervertebral disc (IVD) has increased over recent decades due to their ability to quantify internal stresses and strains throughout the tissue. Their accuracy is dependent upon realistic, strain-rate dependent material properties, which are challenging to acquire.

PURPOSE: The aim of this study was to use the inverse FE technique to characterize the material properties of human lumbar IVDs across strain rates.

STUDY DESIGN: A human cadaveric experimental study coupled with an inverse finite element study.

METHODS: To predict the structural response of the IVD accurately, the material response of the constituent structures was required. Therefore, compressive experiments were conducted on 16 lumbar IVDs (39±19 years) to obtain the structural response. An FE model of each of these experiments was developed and then run through an inverse FE algorithm to obtain subject-specific constituent material properties, such that the structural response was accurate.

RESULTS: Experimentally, a log-linear relationship between IVD stiffness and strain rate was observed. The material properties obtained through the subject-specific inverse FE optimization of the annulus fibrosus (AF) fiber and AF fiber ground matrix allowed a good match between the experimental and FE response. This resulted in a Young modulus of AF fibers (—MPa) to strain rate ($\dot{\varepsilon}$, /s) relationship of YMAF $= 31.5\ln(\dot{\varepsilon}) + 435.5$, and the C_{10} parameter of the Neo-Hookean material model of the AF ground matrix was found to be strain-rate independent with an average value of 0.68 MPa.

CONCLUSIONS: These material properties can be used to improve the accuracy, and therefore predictive ability of FE models of the spine that are used in a wide range of research areas and clinical applications.

CLINICAL SIGNIFICANCE: Finite element models can be used for many applications including investigating low back pain, spinal deformities, injury biomechanics, implant design, design of protective systems, and degenerative disc disease. The accurate material properties obtained in this study will improve the predictive ability, and therefore clinical significance of these models.

Keywords: Finite element method; Intervertebral disc; Lumbar spine; Optimization; Sensitivity; Strain rate

FDA device/drug status: Not applicable.

Author disclosures: ***NN:*** Grant: EPSRC (E), Royal British Legion (I). ***DC:*** Grant: EPSRC (E), Royal British Legion (I). ***GG:*** Grant: EPSRC (E), Royal British Legion (I). ***JPL:*** Nothing to disclose. ***SDM:*** Grant: EPSRC (E), Royal British Legion (I).

* Corresponding author. Department of Bioengineering, Imperial College London, South Kensington Campus, London SW7 2AZ, United Kingdom. Tel.: 07843895728.

E-mail address: n.newell09@imperial.ac.uk (N. Newell).

https://doi.org/10.1016/j.spinee.2019.07.012

Introduction

Lumbar intervertebral discs (IVDs) are complex structures that consist of three main components; the soft, deformable nucleus pulposus (NP), surrounded by the fibrous concentric layers of the annulus fibrosus (AF), and finally, the thin cartilaginous end plates that enclose the NP and AF cranially and caudally. The biomechanics of the IVD have been studied in a wide range of research areas including low back pain, spinal deformities, injury biomechanics, and degenerative disc disease [1]. The majority of these studies have been in vivo or in vitro; however, the use of finite element (FE) methods has increased due to their ability to quantify internal stresses and strains throughout the tissue [2]. The accuracy of the FE models of the spine is dependent upon realistic, strain-rate dependent material properties, which are challenging to acquire.

Spinal models are commonly used to predict loading responses during activities of daily living, both at high and low rates of loading, and therefore it is important to quantify loading rate effects on the IVDs response. Strain rate effects have previously been investigated in animal IVDs [3–5], human IVDs [6–8], and on components of the IVD such as single lamella samples from the human AF [9]. These studies have found an increase in stiffness with strain rate; however, none of these studies provided strain-rate dependent material properties that can be readily used in models of human IVDs.

Traditionally, material properties have been obtained through coupon testing; single lamella layers of the AF have been excised and tested in tension and in shear; the NP has been tested in confined compression; and the end plates have been tested using nanoindentation [1]. These methods have provided valuable data to characterize the properties of IVDs; however, there are a number of limitations associated with these techniques. First, the removal of surrounding tissues may affect the behavior of the individual components. Second, particularly at high strain rates, gripping, and the application of realistic boundary conditions is challenging. One technique to obtain strain-rate dependent material properties, without having to excise individual IVD components or needing to grip the excised samples, is to use an inverse FE approach. This approach has been used to characterize a number of soft tissues, including, the heel fat pad [10,11], the lung [12], the cornea [13], and recently bovine IVDs [4]. This technique involves developing an FE model of the whole system (such as the whole IVD) and optimizing material properties of the individual components to ensure good agreement between the experimental data and FE results.

The aim of this study was to use the inverse FE technique to characterize the material properties of human lumbar IVDs across strain rates.

Methods

Compressive experiments on IVDs were conducted, for each of which an FE model was developed. The inverse FE algorithm was then employed to obtain subject-specific material properties.

Experiments

Sample preparation

Sixteen, fresh frozen, human cadaveric vertebral body-disc-vertebral body (VB-disc-VB) samples were obtained from four male donors (L1–L5) aged 22 to 58 years (mean±standard deviation=40±18 years). Two younger and two older specimens were used for this study to ensure a range of IVD degeneration levels. Ethical approval was obtained from the Tissue Management Committee of the Imperial College Tissue Bank ethics committee (ethical approval number: 12/WA/0196). Samples were sealed and frozen at −20°C. Each spine was scanned using a computed tomography (CT) scanner (IVIS SpectrumCT Imaging System, Caliper Life Sciences, Hopkinton, MA, USA—voxel size 0.15×0.15×0.15 mm) to ensure samples did not have relevant pathology, such as herniations or fractures. A phantom (QRM-BDC, QRM GmbH, Möhrendorf, Germany) was included in the scan. Sagittal magnetic resonance imaging scans of each sample (3T Magnetom Skyra, Siemens, Erlangen, Germany—T2-weighted turbo spin echo sequence, time to repetition=12,730 milliseconds, time to echo=105 milliseconds, flip angle=160°, voxel size 1.0×1.0×5.0 mm) were taken and used to assess the level of disc degeneration using the Pfirrmann scale [14]. Each IVD was ranked by three observers and an average score was calculated.

Before testing, each spine was thawed overnight at room temperature. Soft tissues were removed and the lumbar spine was sectioned into four VB-disc-VB samples with anterior and posterior longitudinal ligaments kept intact and posterior elements removed. After preparation, each sample was wrapped in a paper towel soaked with phosphate buffered saline (0.15 m/L) to keep it hydrated.

The IVDs from all lumbar-spine levels were harvested from each specimen by cutting midway through the cranial and caudal vertebrae. Due to the curvature of the spine, parallel cuts were not always possible. Therefore, following sectioning, samples were CT scanned for a second time. The vertebrae from these scans were segmented in Mimics (Materialise HQ, v.17.0, Leuven, Belgium) using a threshold of 300 Hounsfield units [15–18]. The resulting surface geometry was imported into Geomagic Design X (v.2013.1.1; Geomagic, Inc, Research Triangle Park, NC, USA), where measurements of the angle between the cranial and caudal mid-vertebral transverse cuts were made. Based on these measurements, 3D printed wedges were designed to be positioned above and below

each sample to ensure that the mid-plane of each IVD was perpendicular to the axis of loading. The angle of the wedges was 3.9±2.2° (mean±1 standard deviation). Using a custom-built alignment jig, the samples were fixed in position using polymethyl-methacrylate bone cement.

Experimental procedure

The potted samples were placed into a servohydraulic materials testing machine (8872; Instron, Canton, MA, USA). A custom-designed hood was placed on top of the samples to allow the compressive load to be spread across the pot (Fig. 1). The cross-head was lowered until a small compressive load (50 N) was recorded indicating that the compression tup was in contact with the top pot. The maximum displacement of the cross-head was determined by the target strain for each sample and according to the average central IVD height measured by three different observers from CT scans. The sample was subjected to four compression cycles to 15% strain. Preliminary investigations indicated that 15% strain would not damage the IVDs, thus enabling multiple tests on a single sample. Each IVD was compressed at four strain rates (0.001, 0.01, 0.1, and 1/s). These rates were chosen so that properties could be provided for a range of loading scenarios, from low rate activities of daily living to high rate, potentially injurious situations. Preliminary investigations showed that a 5-minute relaxation period between tests was sufficient to obtain a repeatable force-displacement response.

During the experiments, load was measured using a 10-kN load cell above the compression tup, vertical displacement was measured using two 10-mm stroke linear variable displacement transducers (LVDTs, Model D6/05000A, RDP Electronics Ltd, Wolverhampton, United Kingdom) attached to the top pot, and pressing against 3D printed blocks on the bottom pot. An average of the measurements from each of the LVDTs was used to determine the axial deformation of the sample. Finally, a 1.3-mm diameter pressure needle (Model 8CT/4F/SS/HP, Gaeltec Devices Ltd, Isle of Skye, United Kingdom) was inserted into the NP of each sample through the anterolateral portion of the AF. A 20-G guide needle (0.9-mm diameter) was initially inserted to form the path for the pressure needle. The pressure transducer was aligned to measure in the cranial direction at the center of the NP.

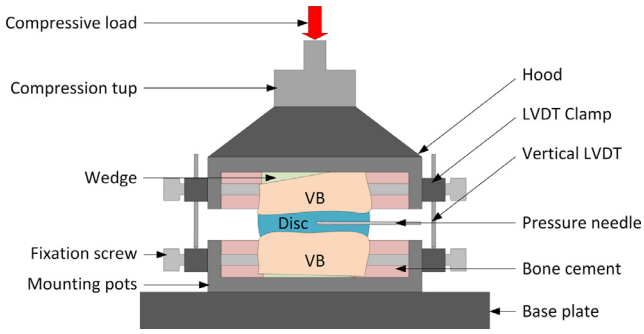

Fig. 1. Diagram of the test setup. VB, vertebral body; LVDT, linear variable displacement transducer.

FE model development

Geometry

The geometry for each of the 16 subject-specific models can be seen in Fig. 2. Each geometry was obtained using a technique that involves selecting key bony anatomical landmarks from CT scans, which are then used to generate meshed parametric representations of samples [19–21]. Within the IVD, the NP size was set to have a transverse cross-sectional area that was 29% of the total cross-sectional area of the IVD. This was chosen because the weighted average cross-sectional area of 59 measurements made in five previous studies investigating lumbar IVDs was 29.1±8.3% (mean±standard deviation) [22–26]. The AF consisted of a matrix, and 20 rebar layers, at ±30° to the transverse plane to represent the layers of collagen fiber bundles [27]. Rebars were embedded every 4.35 mm [27], and their area was adjusted to ensure that 17.8% of the AF volume was taken up by collagen fibers. This value was based on the weighted average AF fiber volume of 276 measurements made in six previous studies investigating nondegenerate lumbar IVDs that was 17.8±7.7% (mean ± standard deviation, note that the AF water content was assumed to be 70% in studies where only percentage dry weight was reported) [28–33]. The cartilage end plate (CEP) was represented by 0.58-mm thick shell elements, above and below the IVD (weighted average of 87 measurements made in three previous studies of human lumbar end plates [32,34,35]). The cortical bone was modeled using 0.78-mm thick quadrilateral shell elements (weighted average of 474 measurements made in five previous studies of human lumbar end plates [36–40]), and trabecular bone was represented by hexahedral, solid elements.

Material properties

The NP was modeled as an incompressible cavity with an initial pressure taken from the experimental measurements. The AF ground matrix was assigned nonlinear elastic properties modeled using an incompressible Neo-Hookean constitutive model (C_{10}=0.436 MPa). These values were obtained by fitting a material model to the average stress-strain response used in previous FE models (Fig. 3).

The rebar elements that represent the collagen-fiber bundles were assigned tension-only linearly elastic properties with a Young modulus of 382.7 MPa (Fig. 4). This value was based on an average of common properties from other FE studies [41–49].

Cartilaginous end plates were assigned linearly elastic material properties with a Young modulus of 23.8 MPa and a Poisson ratio of 0.4 [44,50,51]. Cortical and trabecular bone were assigned linearly elastic properties with a Young modulus of 17.4 GPa and 181 MPa, respectively. The cortical bone properties were based on a nanoindentation study

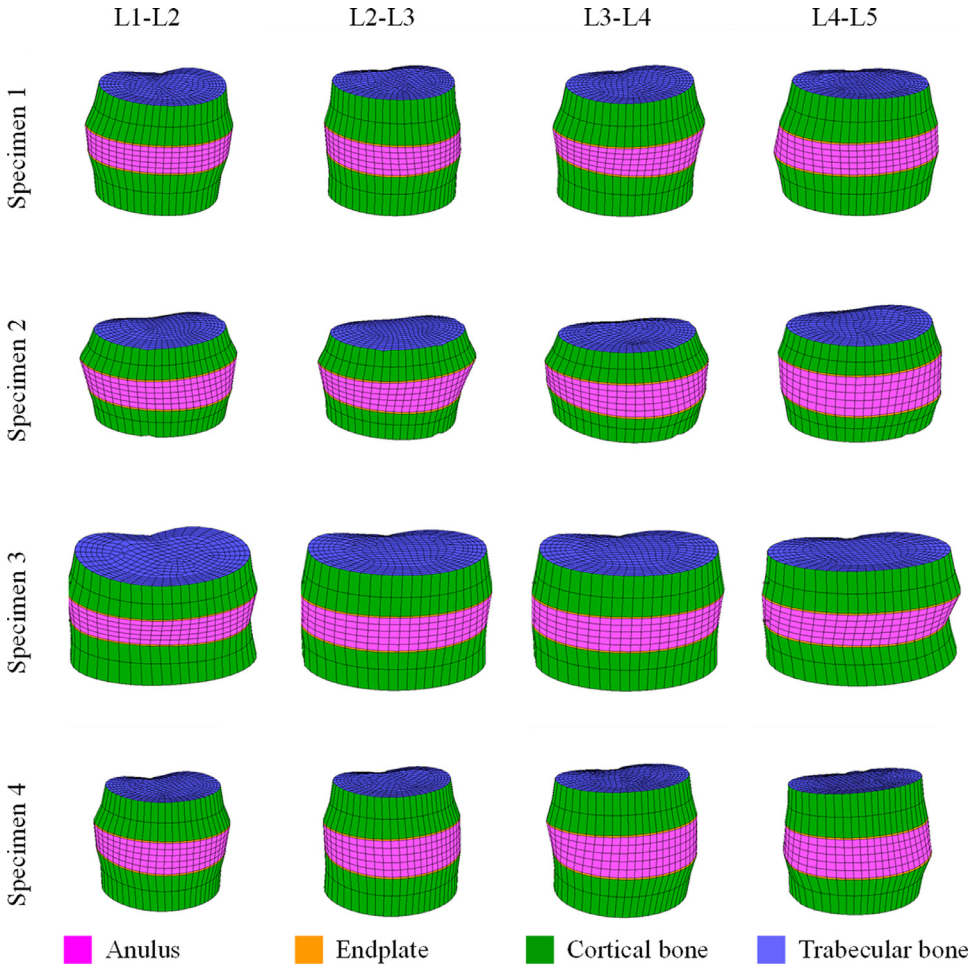

Fig. 2. Diagram showing the geometry of the 16 samples.

performed by Roy et al. [52] whereas the trabecular properties were based on 1,061 measurements made from human vertebrae in 14 previous studies [53–66]. Trabecular bone was assigned a Poisson ratio of 0.28 based on a weighted average of 58 measurements from two studies [64,65], whereas cortical bone was assigned a Poisson ratio of 0.3 which has been commonly used in previous finite element studies [42,45,67].

Boundary conditions

As with the experimental set-up, the inferior boundary of the caudal vertebra was fixed. The axial displacement, measured experimentally by the vertical LVDTs was applied to the superior boundary of the cranial vertebra. All contacts applied in the model (AF and NP, AF and CEP, CEP and cortical bone, cortical bone and trabecular bone, bone and boundaries) were "glued" meaning that no relative motion was allowed between the two surfaces in contact. Force was measured at the upper surface and pressure in the cavity.

Sensitivity study

To determine the contribution of each material property to the overall response of the IVD, a combined sensitivity study was performed on all 16 models at an intermediate strain rate (0.1/s). Ten material and 4 geometric properties were adjusted to the bounds detailed in Table 1 resulting in a total of 448 runs. The peak force and peak pressure were compared with the baseline runs of each model.

Inverse FE modeling

Following the sensitivity study, the values of the material properties that had the greatest effect on the behavior of the model were assumed unknown and were set to be determined using the inverse-FE technique. The initial values and limits of these properties were based on literature values, and an optimization algorithm was employed. The algorithm is based on the derivative-free Nelder-Mead or downhill-simplex method for function minimization [68]. Using the initial values of the modeling properties of interest, computational results were obtained from the model. An objective function was used to calculate the difference between these results and experimental force-time, and pressure-time responses. The properties were then modified and the model rerun to obtain updated results and again compared against the experimental outcome. This was repeated multiple times to minimize the value of the

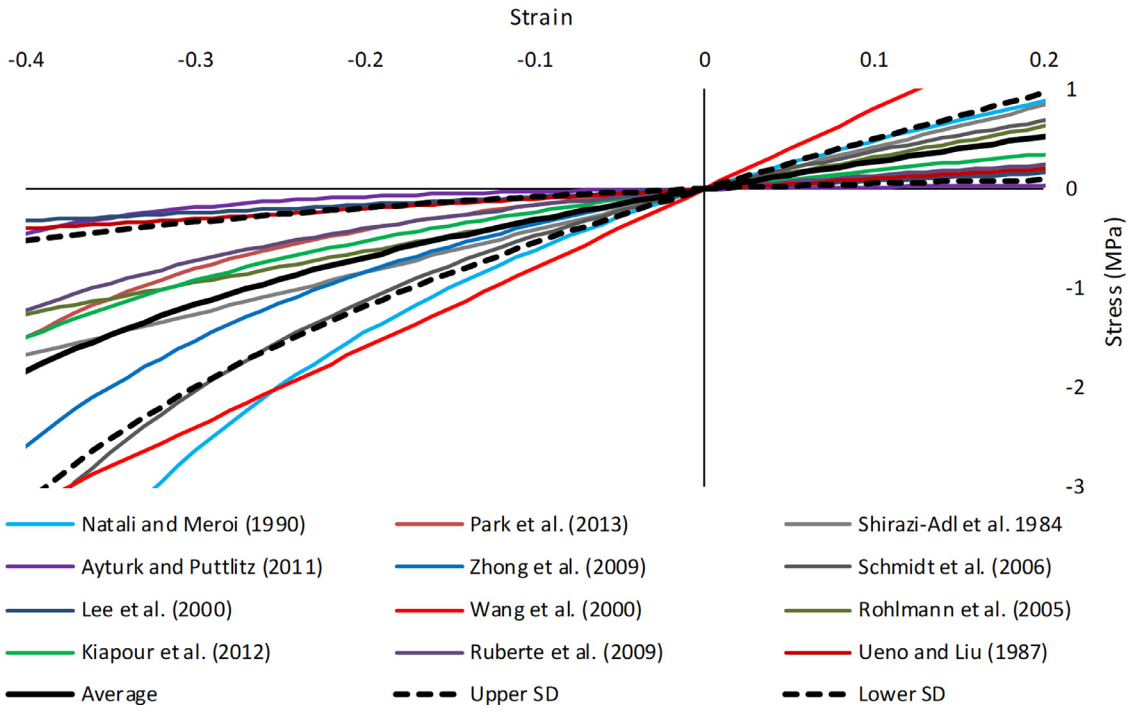

Fig. 3. Material properties of the annulus fibrosus ground matrix used in previous finite element models. An average of the literature values is shown as well as ±1 standard deviation (dotted lines). Neo-Hookean material models were fit to the average (C_{10}=0.436 MPa), upper (C_{10}=0.751 MPa), and lower (C_{10}=0.121 MPa) standard deviation curves for use in the sensitivity study.

objective function until one of the following criteria was met: alterations of the material properties had an effect smaller than 10^{-5} on the objective function; the difference between material properties suggested through consecutive optimization iterations was less than 10^{-5}; or the number of optimization iterations reached 5,000. This optimization process resulted in material properties for each sample, at each strain rate. In addition, normalized root-mean-square deviation (NRMSD) was calculated (Equation (1)) to quantify the goodness of fit between the optimized FE force-time and pressure-time curves, and the experimentally measured data.

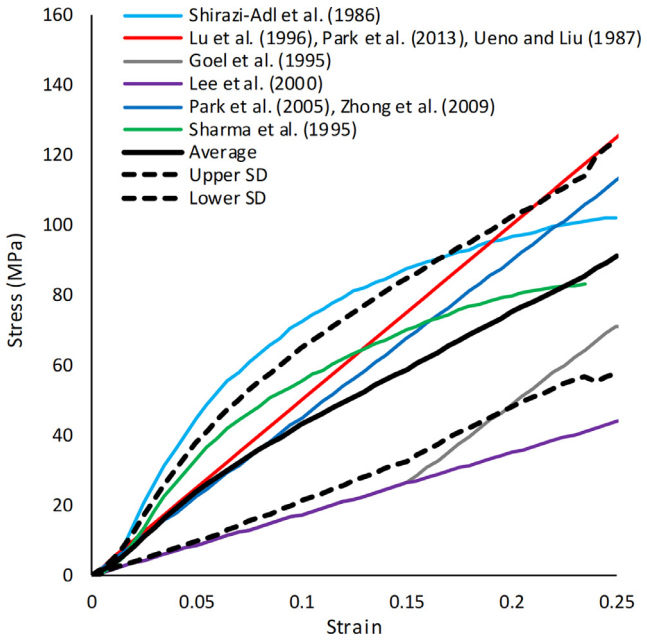

Fig. 4. Material properties of the AF fiber bundles commonly used in finite element models of the IVD with a fitted mean±standard deviation curve. A linear material model was fit to the average (Young modulus, YM=382.7 MPa [R^2=0.98]), upper (YM=534.1 MPa [R^2=0.94]), and lower (YM=231.4 MPa [R^2=0.99]) standard deviation curves for use in the sensitivity study.

$$\mathrm{NRMSD} = \sqrt{\frac{\sum_{i=1}^{n}(Y_i - y_i)^2}{n}}\frac{}{\bar{y}} \quad (1)$$

where Y_i represents the FE values, y_i the experimental values, n the number of data points, and $\bar{y}$ the mean of the experimental values.

Results

Sample details

Sample details including IVD height measured from the CT scans and Pfirrmann rank measured from magnetic resonance imaging scans are shown in Table 2. A range of degeneration grades were represented through the 16 samples (1x grade 1, 7x grade 2, 3x grade 3, and 5x grade 4).

Experimental results

Experimental data are openly available from Mendeley Data [69]. Due to the nonlinear behavior of the IVD, the tangent of the stiffness-axial load and pressure-axial load

Table 1
Initial, and upper and lower bounds of (a) the material and (b) the geometric properties used in the sensitivity study

(a) Material properties

Material property	Initial value	SD/±20%	Upper bound	Lower bound	References
AF C_{10} (MPa)	0.436	SD	0.751	0.121	[43,44,47,67, 79–86]
End plate YM (MPa)	23.8	±20%	28.56	19.04	[44,50,51]
End plate PR	0.4	±20%	0.48	0.32	[44,50,51]
Cortical bone YM (MPa)	17420	SD	20300	14500	[52]
Cortical bone PR	0.3	±20%	0.36	0.24	[42,45,67]
Cancellous bone YM (MPa)	181.0	SD	385.2	23.2*	[53–66]
Cancellous bone PR	0.28	SD	0.56	0.0	[64,65]
Fiber YM (MPa)	382.7	SD	721.8	145.5	[41–49]
Fiber PR	0.35	±20%	0.36	0.24	[44]
Cavity pressure (kPa)	386	SD	678	92	[87–89]

(b) Geometric properties

Geometric property	Initial value	SD/±20%	Upper bound	Lower bound	References
Fiber volume (% of AF)	17.8	SD	25.5	10.1	[28–33]
Rebar angle (°)	27.0	SD	32.5	21.6	[26,28,90,76,77,91]
Cartilage end plate thickness (mm)	0.58	SD	0.83	0.33	[32,34,35]
Bony end plate thickness (mm)	0.78	SD	1.17	0.39	[36–40]

AF, annulus fibrosus; YM, Young modulus; PR, Poisson ratio.
Where values were available, the initial values were adjusted by ±1 standard deviation (SD), otherwise values were adjusted by ±20%.
* The standard deviation for the cancellous bone Young modulus was 204.3 MPa which would have resulted in a negative lower bound; therefore, the lowest average from the cited papers was used 56.

graphs was calculated at three strains: 4%, 8%, and 12%. No significant differences were seen across spinal levels at any strain ($p>.05$) and therefore the data from each level were grouped for further analysis. The IVD stiffness increased with strain rate at all three strains, with stiffness (k, kN/mm)–strain-rate ($\dot{\varepsilon}$,/s) relationships of $k = 37.96\ln(\dot{\varepsilon}) + 1147.91$, $k = 67.04\ln(\dot{\varepsilon}) + 2117.59$, and $k = 116.94\ln(\dot{\varepsilon}) + 3810.55$, for 4%, 8%, and 12% strain, respectively ($R^2 = 0.97$, $R^2 = 0.97$, and $R^2 = 0.99$, respectively).

Table 2
Sample details

Sample #	Age (y)	Level	Pfirrmann grade	Central IVD height (mm)
1.1	58	L1–L2	3	9.5±0.3
1.2		L2–L3	3	9.3±0.4
1.3		L3–L4	4	9.7±0.0
1.4		L4–L5	3	10.9±0.6
2.1	22	L1–L2	1	9.1±0.1
2.2		L2–L3	2	11.1±0.5
2.3		L3–L4	2	12.8±0.3
2.4		L4–L5	2	12.1±0.3
3.1	53	L1–L2	4	8.8±0.2
3.2		L2–L3	4	9.3±0.3
3.3		L3–L4	4	9.9±0.2
3.4		L4–L5	4	9.1±0.2
4.1	23	L1–L2	2	7.3±0.1
4.2		L2–L3	2	10.7±0.0
4.3		L3–L4	2	11.8±0.2
4.4		L4–L5	2	12.2±0.4

Pfirrmann grades are rounded averages of rankings made by three observers. IVD heights (±1 standard deviation) are an average of three measurements at the center of the IVD.

The average pressure within the NP before loading was measured to be 78.5±52.54 kPa (mean±standard deviation). A linear, strain, and strain-rate independent relationship was seen between axial load and NP pressure of 0.85± 0.18 MPa/kN (Fig. 6).

FE models

Sensitivity

An overview of the results of the sensitivity study is shown in Fig. 7. The C_{10} parameter of the AF ground matrix, Young modulus of the AF fibers (YMAF), volume of the AF fibers, thickness of the CEP, and pressure in the NP had the greatest effects on the model (on average, >5% change from the baseline in either peak force or peak NP pressure). Of these, the C_{10} parameter of the AF ground matrix and the YMAF were chosen as the variables to be adjusted in the optimization study. Because the model was sensitive to the pressure of the NP, the experimentally measured values were used rather than values from literature. Additionally, the Young modulus of cancellous bone was assigned subject-specific values based on the average Hounsfield units of the trabecular bone in each vertebra taken from the CT scans [57]. Although the AF fiber volume had a relatively large effect on the model's response, it was not optimized due to its linear correlation with the YMAF bundles. The thickness of the CEP was not optimized because the geometry of the subject-specific models had IVD heights based on the selection of landmarks from CT scans, and therefore adjusting the thickness of the CEP would have resulted in inaccurate IVD heights.

Optimization

The initial material properties used in the optimization were the same as those used in the sensitivity study and presented in Table 1. Fig. 8 shows the goodness-of-fit NRMSD values between the experimental and FE force-time (Top), and pressure-time (Bottom) curves for each sample, at each strain rate. Average NRMSDs were lower for the force-time curves in comparison to the pressure-time curves (average 0.11±0.09 vs. 0.39±0.32, respectively).

The average optimized YMAF and the C_{10} parameter of the AF ground matrix are shown in Fig. 9. An increase in optimized YMAF was seen with strain rate, with a log-linear relationship of $YMAF = 31.5\ln(\dot{\varepsilon}) + 435.5$ (R^2=0.95). The optimized C_{10} parameter of the AF ground matrix did not have a clear strain rate dependent relationship (Fig. 9, Right). The average C_{10} parameter of the AF ground matrix was 0.068±0.06 MPa across all specimens, and all strain rates.

Discussion

Experimental results

The experiments conducted in this study are the first to measure IVD force-time, and NP pressure-time behaviors at a range of strain rates in human samples. In agreement with previous studies [3,4,7,8], an increase in IVD stiffness was seen with increased strain rates (Fig. 5). The log-linear relationships shown in Fig. 5 support the findings of Race et al. [3] who reported a threshold above which the strain rate sensitivity in stiffness was negligible in animal IVDs, although a discrete value for this threshold was not identified in this study. On average, a 1,000-times increase in strain rate (from 0.001/s to 1/s) caused a 30.8±8.4% increase in stiffness at 12% strain, demonstrating the importance of considering strain rate when predicting the response of an IVD, particularly when modeling activities of daily living that load the IVD at a range of strain rates. However, the experimental data show that the interspecimen response is an even more important parameter to consider when developing subject-specific FE models, demonstrated by the sixfold increase in stiffness seen between the softest, and stiffest specimen at 12% strain, and at an intermediate strain rate (0.1/s). This highlights the need to use subject-specific material properties to accurately capture the response of a specific IVD using FE modeling. It also shows that care needs to be taken when extrapolating to a large population the results obtained on an average geometry model of the IVD, as has also been found in FE models of other body regions such as the hip [70].

The relationship between NP pressure and load in this study (0.85±0.17 MPa/kN) was comparable to that found by Brinckmann and Grootenboer [71] (0.97±0.24 MPa/kN). They tested 19 human lumbar IVDs and measured IVD pressure at discrete load steps, although they did not investigate the strain-rate dependence of this relationship.

Inherent with studies of this kind, a potential limitation is sample size. Here we used 16 IVDs from four donors which was enough to obtain rate dependent stiffnesses for this inverse-FE study and is within the range of sample sizes used in other studies that have investigated strain rate effects in IVDs—17.5±17.2 IVDs (mean±standard deviation, range 7–52 IVDs) [3–8]. However, a future study with a larger sample size may uncover differences in IVD stiffness due to level of degeneration, or lumbar level.

Sensitivity

The sensitivity study was conducted on all 16 geometrically subject-specific FE models. To our knowledge, this is the largest set of subject-specific models on which a study of this kind has been conducted. The sensitivity results were broadly in agreement with previous studies which, in general, have found that IVD models are sensitive to soft tissue properties, but not hard tissue properties [72–75]. Understandably, there have been differences in the relative

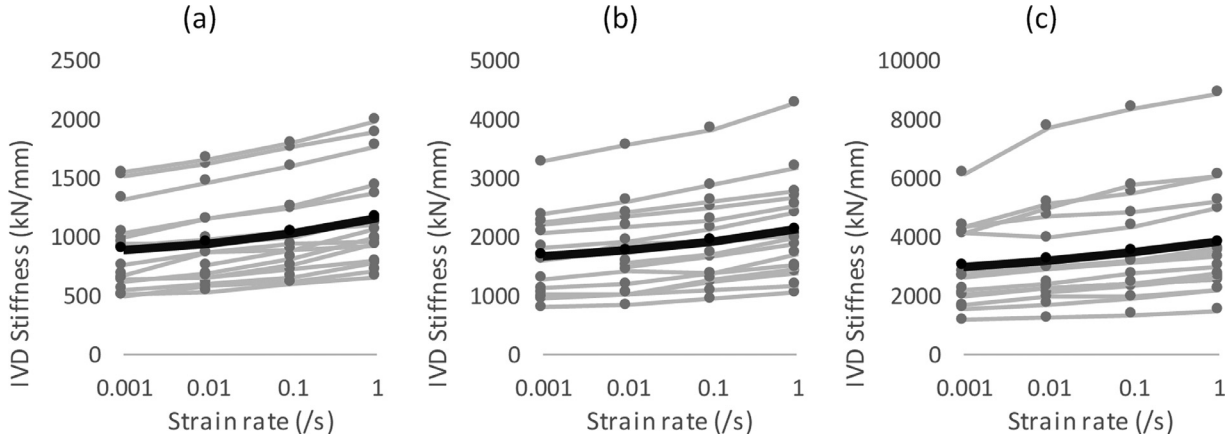

Fig. 5. Intervertebral disc stiffness versus logarithmic strain rate at (Left) 4%, (Middle) 8%, and (Right) 12% strain. Gray lines represent individual samples and the thick black line represents an average of all samples at each strain rate.

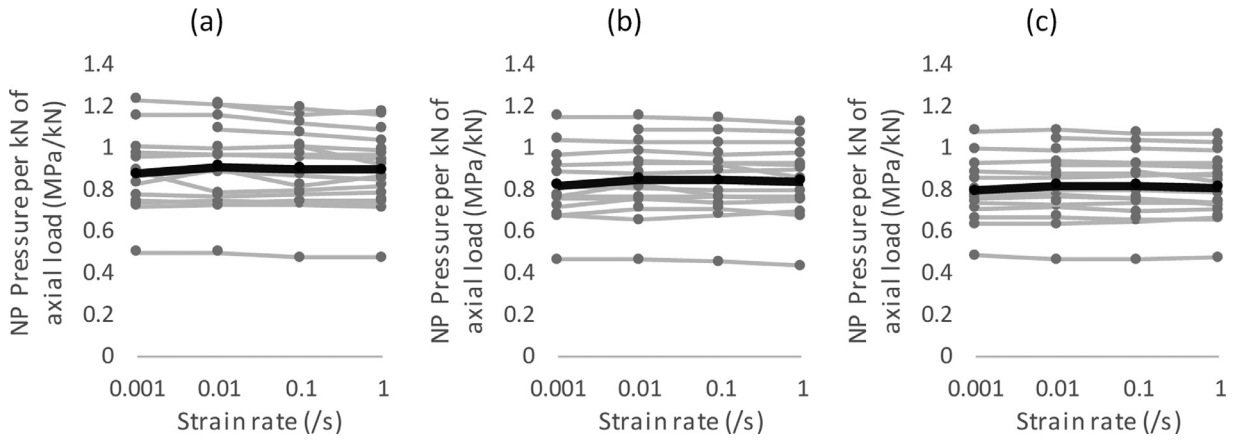

Fig. 6. Nucleus pulposus pressure per kN of axial load versus logarithmic strain rate at (Left) 4%, (Middle) 8%, and (Right) 12% strain. Note that data for specimen 3.3 at 0.001/s and 0.01/s were removed due to errors in the pressure readings.

importance of AF ground matrix, AF fibers, and the NP properties in previous studies because they are dependent on the initial stiffness values of each material; for example, if the ground matrix is stiffer than the fibers, it is likely to play a greater role in the load transfer. In this study, cancellous bone properties were found to influence the IVD behavior under load, likely due to the change in the degree of end plate bulging. This effect was also seen in the axisymmetric sensitivity study performed by Suwito et al. [74]. Here, the CEP thickness was altered by shifting the VBs away from the IVD to allow the CEP thickness to increase, thus increasing the IVD height, which has been shown to affect model response in other studies [42]. The effect of CEP Young modulus was less pronounced and probably a more realistic indicator of the importance of CEP properties on the response of the IVD.

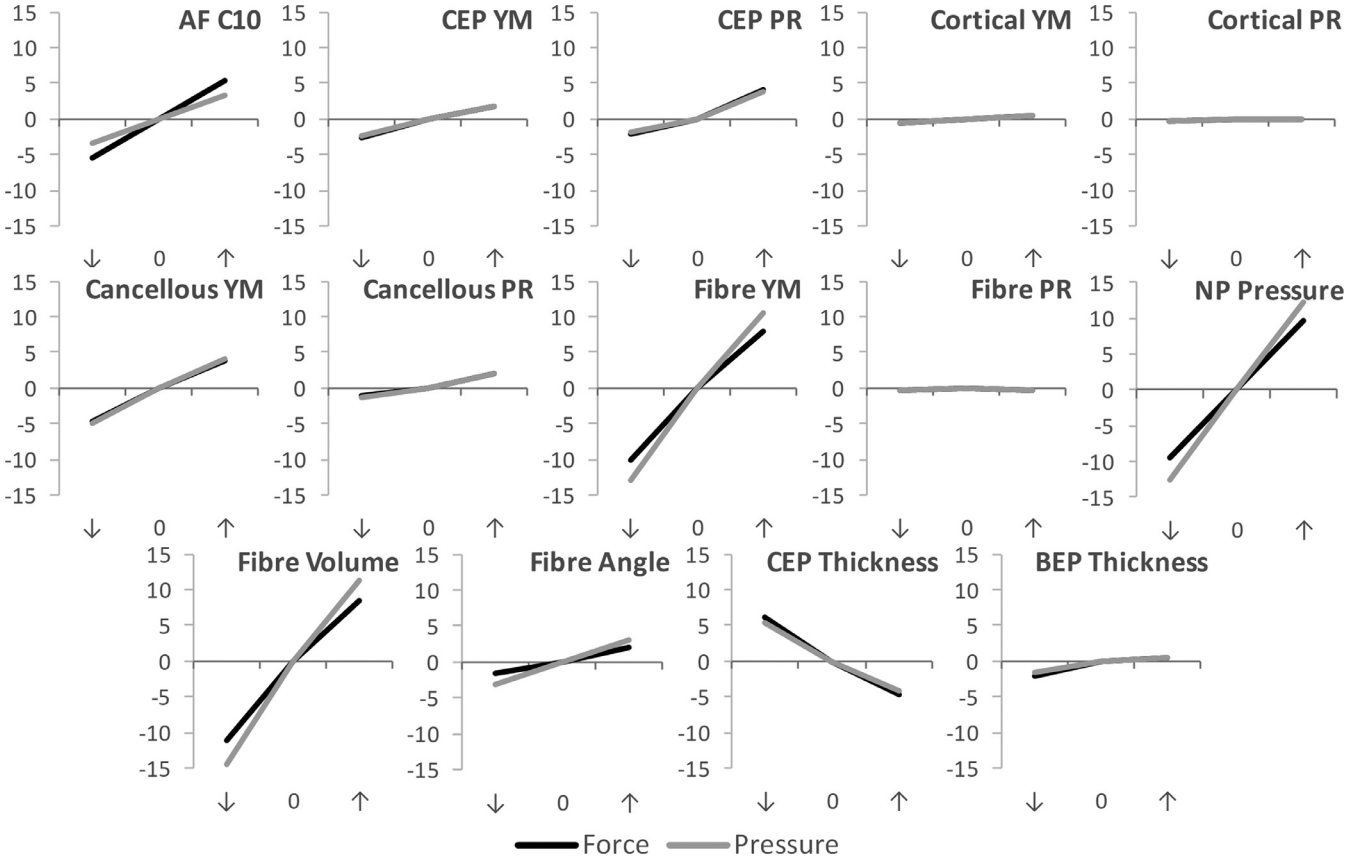

Fig. 7. Overview of the results of the sensitivity study. The y-axis represents a percentage change from the peak force and peak nucleus pulposus pressure calculated from the baseline model when the variable was increased (↑) or decreased (↓) to the bounds shown in Table 1. AF, annulus fibrosus; NP, nucleus pulposus; CEP, cartilage end plate; BEP, bony end plate; YM, Young modulus; PR, Poisson ratio.

A limitation of this sensitivity study is that one variable was altered at a time and so combined effects may have been missed. The purpose of this sensitivity study was to identify properties to be optimized and therefore altering one parameter at a time was deemed appropriate. A probabilistic or factorial analysis may be more useful for studies that aim to understand the effects of different combinations of parameters on the IVD response.

Optimization

There was a close match between experimental and FE responses following optimization of the AF fibers and AF ground matrix material properties demonstrating that the compressive behavior of an IVD can be captured by determining these two parameters. There was a closer match in the force-displacement response compared with the pressure-displacement response; this could be partly due to the consistent NP:AF ratio in all models.

The significant influence of strain rate on the optimized material properties demonstrates the importance of accounting for these variables when developing FE models. The range of values for YMAF obtained here (200–415 MPa) was within what has been used previously in FE studies (44.–500 MPa; Fig. 4), and a similar inverse-FE technique for bovine samples (277–540 MPa) [4]. The optimized C_{10} parameters of the AF ground matrix (0.060–0.083 MPa) were at the low end but within the range of values in the literature (0.0146–0.7 MPa; Fig. 3).

Geometric simplifications in the FE models used in this study include assuming the same NP:AF ratio, AF fiber volume, number of lamella layers, end plate thickness, and

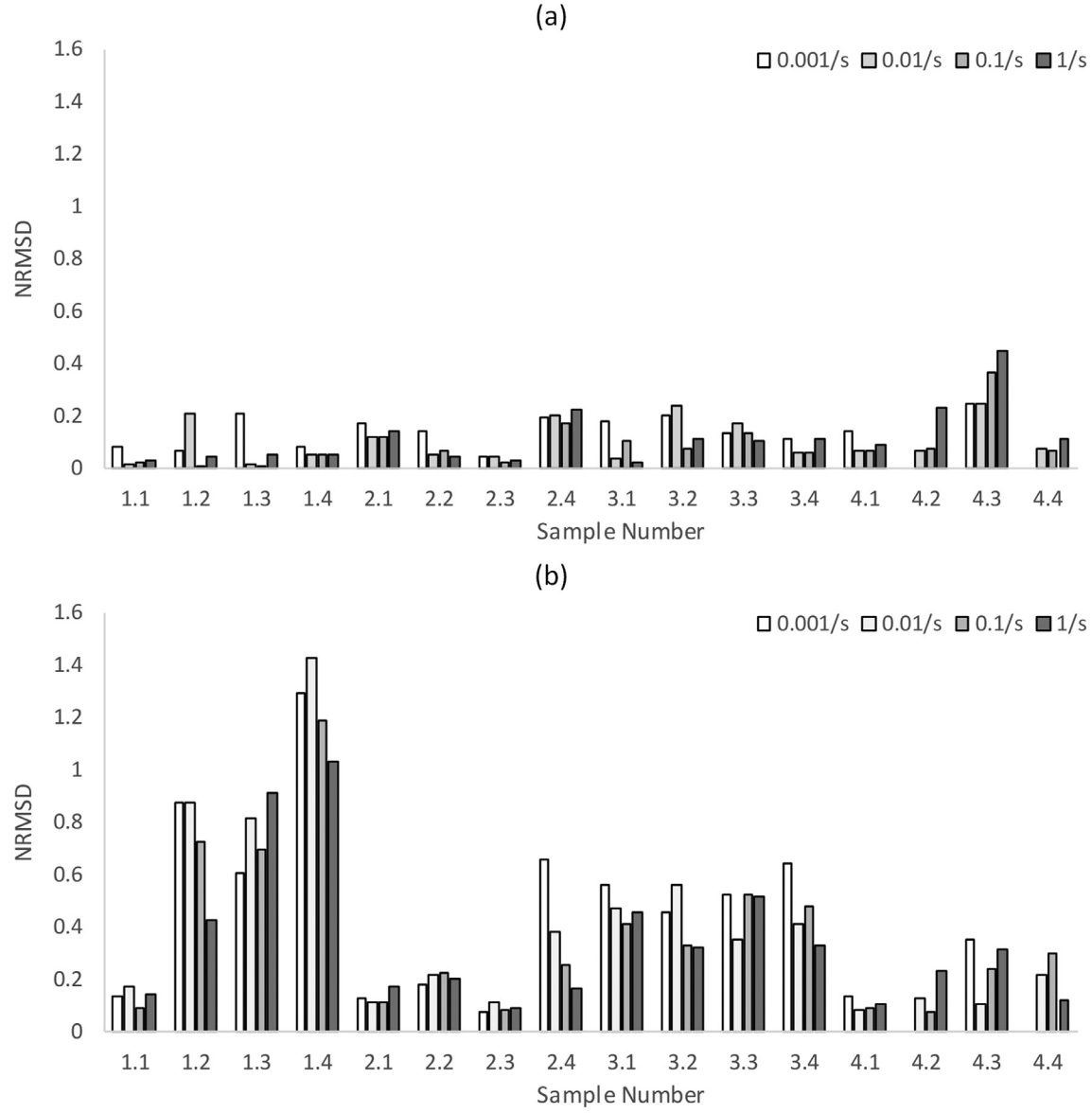

Fig. 8. Normalized root-mean-square deviation (NRMSD) between experimental and optimized FE (Top) force-time, and (Bottom) pressure-time histories.

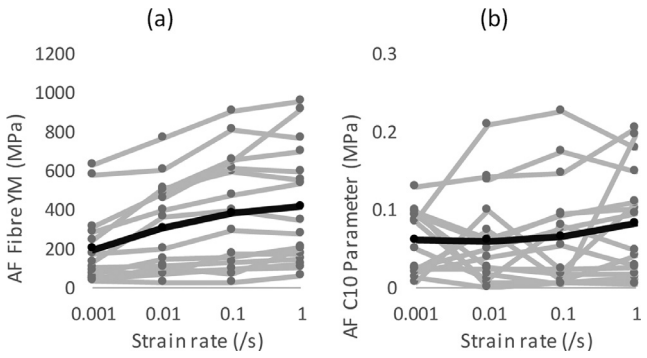

Fig. 9. Optimized (Left) Young modulus of the AF fibers and (Right) C_{10} parameter of the AF ground matrix at each strain rate. Gray lines represent individual samples and the thick black line represents an average of all samples at each strain rate.

cortical bone thickness for all samples. In addition, the angle of the AF fibers was not increasing toward the center of the IVD in the FE models as has been seen physiologically [26,27,76–78]. The effects of most of these geometric differences will have been captured by the optimization of the AF fiber and AF ground matrix material properties, or the effect on the response of the model was small (eg, the cortical [or BEP] bone thickness—Fig. 7); however, the differences between experimental and FE NP pressure-displacement response (Fig. 8, Bottom) in some of the samples shows that the NP:AF ratio may need to be refined for applications where accurate NP pressure values are important. This study has only investigated the response of the IVD under axial compression; therefore, an obvious direction for future work would be to determine whether these properties are valid for use in other modes of loading.

Conclusions

Experimentally, a log-linear relationship between lumbar IVD stiffness and strain rate was observed. Using a subject-specific inverse FE optimization, the YMAF (MPa) to strain rate ($\dot{\varepsilon}$,/s) relationship was determined as $\mathrm{YMAF} = 31.5\ln(\dot{\varepsilon}) + 435.5$, and the C_{10} parameter of the Neo-Hookean material model of the AF ground matrix was found to be strain-rate independent with an average value of 0.68 MPa.

These material properties can be used to improve the accuracy, and therefore predictive ability of FE models of the spine that are used in a wide range of research areas and clinical applications including low back pain, spinal deformities, injury biomechanics, implant design, design of protective systems, and degenerative disc disease.

Acknowledgments

This work was supported by the EPSRC, First Grant Scheme, EP/ M022242/1. Contributions to this work were made under the auspices of The Royal British Legion Centre for Blast Injury Studies at Imperial College London; therefore, the financial support of the Royal British Legion for NN, DC, GG and SM is gratefully acknowledged. Tissue samples were provided by the Imperial College Healthcare NHS Trust Tissue Bank (ICHTB). Other investigators may have received samples from these same tissues. The research was supported by the National Institute for Health Research (NIHR) Biomedical Research Centre based at Imperial College Healthcare NHS Trust and Imperial College London. The views expressed are those of the authors and not necessarily those of the NHS, the NIHR or the Department of Health.

References

[1] Newell N, Little J, Christou A, Adams M, Adam C, Masouros S. Biomechanics of the human intervertebral disc: a review of testing techniques and results. J Mech Behav Biomed Mater 2017;69:420–34.
[2] Schmidt H, Galbusera F, Rohlmann A, Shirazi-Adl A. What have we learned from finite element model studies of lumbar intervertebral discs in the past four decades? J Biomech 2013;46:2342–55.
[3] Race A, Broom ND, Robertson P. Effect of loading rate and hydration on the mechanical properties of the disc. Spine 2000;25:662–9.
[4] Newell N, Grigoriadis G, Christou A, Carpanen D, Masouros SD. Material properties of bovine intervertebral discs across strain rates. J Mech Behav Biomed Mater 2017;65:824–30.
[5] Yingling VR, Callaghan JP, McGill SM. Dynamic loading affects the mechanical properties and failure site of porcine spines. Clin Biomech 1997;12:301–5.
[6] Costi JJ, Stokes IA, Gardner-Morse MG, Iatridis JC. Frequency-dependent behaviour of the intervertebral disc in response to each of six degree of freedom dynamic loading: solid phase and fluid phase contributions. Spine 2008;33:1731–8.
[7] Smeathers JE, Joanes DN. Dynamic compressive properties of human lumbar intervertebral joints: a comparison between fresh and thawed specimens. J Biomech 1988;21:425–33.
[8] Kemper AR, McNally C, Duma SM. The influence of strain rate on the compressive stiffness properties of human lumbar intervertebral discs. Biomed Sci Instrum 2007;43:176–81.
[9] Holzapfel GA, Schulze-Bauer CAJ, Feigl G, Regitnig P. Single lamellar mechanics of the human lumbar anulus fibrosus. Biomech Model Mechanobiol 2005;3:125–40.
[10] Erdemir A, Viveiros M. An inverse finite-element model of heel-pad indentation. J Biomech 2006;39:1279–89.
[11] Grigoriadis G, Newell N, Carpanen D, Christou A, Bull A, Masouros S. Material properties of the heel fat pad across strain rates. J Mech Behav Biomed Mater 2017;65:398–407.
[12] Sadeghi Naini A, Patel RV, Samani A. Measurement of lung hyperelastic properties using inverse finite element approach. IEEE Trans Biomed Eng 2011;58:2852–9.
[13] Nguyen TD, Boyce BL. An inverse finite element method for determining the anisotropic properties of the cornea. Biomech Model Mechanobiol 2011;10:323–37.
[14] Pfirrmann C, Metzdorf A, Zanetti M, Hodler J, Boos N. Magnetic resonance classification of lumbar intervertebral disc degeneration. Spine 2001;26:1873–8.
[15] Sylvestre P-L, Villemure I, Aubin C-E. Finite element modeling of the growth plate in a detailed spine model. Med Biol Eng Comput 2007;45:977–88.
[16] Giambini H, Khosla S, Nassr A, Zhao C, An K-N. Longitudinal changes in lumbar bone mineral density distribution may increase the risk of wedge fractures. Clin Biomech 2013;28:10–4.
[17] Parenteau C, Wang N, Zhang P. Quantification of pediatric and adult cervical vertebra anatomical characteristics by age and gender for automotive application. Traffic Inj Prev Available at: http://www.tandfonline.com/doi/abs/10.1080/15389588.2013.843774. Accessed September 11, 2014.

[18] Gill S, Abolmaesumi P, Fichtinger G, Boisvert J, Pichora D, Borshneck D, et al. Biomechanically constrained groupwise ultrasound to CT registration of the lumbar spine. Med Image Anal 2012;16:662–74.
[19] Little JP, Adam CJ. Geometric sensitivity of patient-specific finite element models of the spine to variability in user-selected anatomical landmarks. Comput Methods Biomech Biomed Engin 2013;18:37–41.
[20] Little JP, De Visser H, Pearcy MJ, Adam CJ. Are coupled rotations in the lumbar spine largely due to the osseo-ligamentous anatomy?—a modeling study. Comput Methods Biomech Biomed Engin 2008;11:95–103.
[21] Little JP, Adam C. Patient-specific computational biomechanics for simulating adolescent scoliosis surgery: predicted vs clinical correction for a preliminary series of six patients. Int. J. Numer. Meth. Biomed. Engng 2011;27:347−56.
[22] Farfan HF, Cossette JW, Robertson GH. The effects of torsion on the lumbar intervertebral joints: the role of torsion in the production of disc degeneration. J Bone Jt Surg 1970;52:468–97.
[23] O'Connell GD, Vresilovic EJ, Elliott DM. Comparison of animals used in disc research to human lumbar disc geometry. Spine 2007;32:328–33.
[24] Perey O. Fracture of the vertebral end-plate in the lumbar spine: an experimental biochemical investigation. Acta Orthop Scand 1957;18:1–101.
[25] Little JP, Pearcy MJ, Pettet GJ. Parametric equations to represent the profile of the human intervertebral disc in the transverse plane. Med Biol Eng Comput 2007;45:939–45.
[26] Pooni J, Hukins D, Harris P, Hilton R, Davies K. Comparison of the structure of human intervertebral discs in the cervical, thoracic and lumbar regions of the spine. Surg Radiol Anat 1986;8:175–82.
[27] Marchand F, Ahmed AM. Investigation of the laminate structure of lumbar disc anulus fibrosus. Spine 1990;15:402–10.
[28] Galante JO. Tensile properties of the human lumbar annulus fibrosus. Acta Orthop Scand 1967;6470(Suppl 100):1–91.
[29] Antoniou J, Steffen T, Nelson F, Winterbottom N, Hollander AP, Poole RA, et al. The human lumbar intervertebral disc: evidence for changes in the biosynthesis and denaturation of the extracellular matrix with growth, maturation, ageing, and degeneration. J Clin Invest 1996;98:996–1003.
[30] Adams P, Eyre DR, Muir H. Biochemical aspects of development and ageing of human lumbar intervertebral discs. Rheumatol Rehabil 1977;16:22–9.
[31] Mikawa Y, Hamagami H, Shikata J, Yamamuro T. Elastin in the human intervertebral disk. A histological and biochemical study comparing it with elastin in the human yellow ligament. Arch Orthop Trauma Surg 1986;105:343–9.
[32] Roberts S, Menage J, Urban J. Biochemical and structural properties of the cartilage end-plate and its relation to the intervertebral disc. Spine 1989;14:166–74.
[33] Skaggs DL, Weidenbaum M, Iatridis JC, Ratcliffe A, Mow VC. Regional variation in tensile properties and biochemical composition of the human lumbar anulus fibrosus. Spine 1994;19:1310–9.
[34] Moon S, Yoder J, Wright A, Smith L, Vresilovic E, Elliott D. Evaluation of intervertebral disc cartilaginous endplate structure using magnetic resonance imaging. Eur Spine J 2013;22:1820–8.
[35] Lama P, Zehra U, Balkovec C, Claireaux HA, Flower L, Harding IJ, et al. Significance of cartilage endplate within herniated disc tissue. Eur Spine J 2014;23:1869–77.
[36] Silva MJ, Wang C, Keaveny TM, Hayes WC. Direct and computed tomography thickness measurements of the human, lumbar vertebral shell and endplate. Bone 1994;15:409–14.
[37] Roberts S, McCall IW, Menage J, Haddaway MJ, Eisenstein SM. Does the thickness of the vertebral subchondral bone reflect the composition of the intervertebral disc? Eur Spine J 1997;6:385–9.
[38] Thomas Edwards W, Zheng Y, Ferrara LA, Yuan HA. Structural features and thickness of the vertebral cortex in the thoracolumbar spine. Spine 2001;26:218–25.
[39] Zhao FD, Pollintine P, Hole BD, Adams MA, Dolan P. Vertebral fractures usually affect the cranial endplate because it is thinner and supported by less-dense trabecular bone. Bone 2009;44:372–9.
[40] Wang Y, Battié MC, Boyd SK, Videman T. The osseous endplates in lumbar vertebrae: thickness, bone mineral density and their associations with age and disk degeneration. Bone 2011;48:804–9.
[41] Shirazi-Adl A, Ahmed AM, Shrivastava SC. A finite element study of a lumbar motion segment subjected to pure sagittal plane moments. J Biomech 1986;19:331–50.
[42] Lu YM, Hutton WC, Gharpuray VM. Do bending, twisting, and diurnal fluid changes in the disc affect the propensity to prolapse? A viscoelastic finite element model. Spine 1996;21:2570–9.
[43] Park WM, Kim K, Kim YH. Effects of degenerated intervertebral discs on intersegmental rotations, intradiscal pressures, and facet joint forces of the whole lumbar spine. Comput Biol Med 2013;43:1234–40.
[44] Ueno K, Liu YK. A three-dimensional nonlinear finite element model of lumbar intervertebral joint in torsion. J Biomech Eng 1987;109:200–9.
[45] Goel VK, Ramirez S a, Kong W, Gilbertson LG. Cancellous bone Young's modulus variation within the vertebral body of a ligamentous lumbar spine—application of bone adaptive remodeling concepts. J Biomech Eng 1995;117:266–71.
[46] Lee CK, Kim YE, Lee CS, Hong YM, Jung JM, Goel VK. Impact response of the intervertebral disc in a finite-element model. Spine 2000;25:2431–9.
[47] Zhong ZC, Chen SH, Hung CH. Load- and displacement-controlled finite element analyses on fusion and non-fusion spinal implants. Proc Inst Mech Eng H 2009;223:143–57.
[48] Sharma M, Langrana NA, Rodriguez J. Role of ligaments and facets in lumbar spinal stability. Spine 1995;20:887–900.
[49] Park WM, Park Y-S, Kim K, Kim YH. Biomechanical comparison of instrumentation techniques in treatment of thoracolumbar burst fractures: a finite element analysis. J Orthop Sci 2009;14:443–9.
[50] Belytschko T, Kulak RF, Schultz a B, Galante JO. Finite element stress analysis of an intervertebral disc. J Biomech 1974;7:277–85.
[51] Yamada H. Strength of biological materials. Baltimore, MD, USA: Williams & Wilkins; 1970. https://doi.org/10.1016/0021-9290(71)90027-3.
[52] Roy ME, Rho JY, Tsui TY, Evans ND, Pharr GM. Mechanical and morphological variation of the human lumbar vertebral cortical and trabecular bone. J Biomed Mater Res 1999;44:191–7.
[53] Lindahl O. Mechanical properties of dried defatted spongy bone. Acta Orthop 1976;47:11–9.
[54] Augat P, Link T, Lang TF, Lin JC, Majumdar S, Genant HK. Anisotropy of the elastic modulus of trabecular bone specimens from different anatomical locations. Med Eng Phys 1998;20:124–31.
[55] Goulet RW, Goldstein SA, Ciarelli MJ, Kuhn JL, Brown MB, Feldkamp LA. The relationship between the structural and orthogonal compressive properties of trabecular bone. J Biomech 1994;27. https://doi.org/10.1016/0021-9290(94)90014-0.
[56] Keller TS, Hansson TH, Abram AC, Spengler DM, Panjabi MM. Regional variations in the compressive properties of lumbar vertebral trabeculae. Effects of disc degeneration. Spine 1989;14:1012–9.
[57] Kopperdahl D, Morgan E, Keaveny T. Quantitative computed tomography estimates of the mechanical properties of human vertebral trabecular bone. J Orthop Res 2002;20:801–5.
[58] Uchiyama T, Tanizawa T, Muramatsu H, Endo N, Takahashi HE, Hara T. Three-dimensional microstructural analysis of human trabecular bone in relation to its mechanical properties. Bone 1999;25:487–91.
[59] Nicholson PH, Cheng XG, Lowet G, Boonen S, Davie MW, Dequeker J, et al. Structural and material mechanical properties of human vertebral cancellous bone. Med Eng Phys 1997;19:729–37.

[60] Morgan EF, Bayraktar HH, Keaveny TM. Trabecular bone modulus-density relationships depend on anatomic site. J Biomech 2003;36:897–904.
[61] Banse X, Sims TJ, Bailey AJ. Mechanical properties of adult vertebral cancellous bone: correlation with collagen intermolecular cross-links. J Bone Miner Res 2002;17:1621–8.
[62] Kim DG, Hunt CA, Zauel R, Fyhrie DP, Yeni YN. The effect of regional variations of the trabecular bone properties on the compressive strength of human vertebral bodies. Ann Biomed Eng 2007;35:1907–13.
[63] Hou FJ, Lang SM, Hoshaw SJ, Reimann DA, Fyhrie DP. Human vertebral body apparent and hard tissue stiffness. J Biomech 1998;31:1009–15.
[64] McElhaney J, Alem N, Roberts V. A porous block model for cancellous bone. Trans ASME. 1970:1–9.
[65] Yahia LH, Drouin G, Duval P. A methodology for mechanical measurements of technical constants of trabecular bone. Eng Med 1988;17:169–73.
[66] Kabel J, Odgaard A, Van Rietbergen B, Huiskes R. Connectivity and the elastic properties of cancellous bone. Bone 1999;24:115–20.
[67] Shirazi-Adl SA, Shrivastava SC, Ahmed AM. Stress analysis of the lumbar disc-body unit in compression. A three-dimensional nonlinear finite element study. Spine 1984;9:120–34.
[68] Nelder J, Mead R. A simplex method for function minimization. Comput J 1965;7:308–13.
[69] Newell N. Material properties of human lumbar intervertebral discs across strain rates—experimental data. Mendeley Data 2019. http://dx.doi.org/10.17632/29hd3mdfyc.1.
[70] O'Rourke D, Bottema M, Taylor M. Sampling strategies for approximating patient variability in population-based finite element studies of total hip replacement. Int J Numer Method Biomed Eng 2018:e3168.
[71] Brinckmann P, Grootenboer H. Change of disc height, radial disc bulge, and intradiscal pressure from discectomy. An in vitro investigation on human lumbar discs. Spine 1991;16:641–6.
[72] Kumaresan S, Yoganandan N, Pintar FA. Finite element analysis of the cervical spine: a material property sensitivity study. Clin Biomech 1999;14:41–53.
[73] Fagan MJ, Julian S, Siddall DJ, et al. Patient-specific spine models. Part 1: finite element analysis of the lumbar intervertebral disc—a material sensitivity study. Proc Inst Mech Eng Part H 2002;216:299–314.
[74] Suwito W, Keller TS, Basu PK, et al. Geometric and material property study of the human lumbar spine using the finite element method. J Spinal Disord 1992;5:50–9.
[75] Rao AA, Dumas GA. Influence of material properties on the mechanical behaviour of the L5-S1 intervertebral disc in compression: a non-linear finite element study. J Biomed Eng 1991;13:139–51.
[76] Cassidy JJ, Hiltner A, Baer E. Hierarchical structure of the intervertebral disc. Connect Tissue Res 1989;23:75–88.
[77] Hsu EW, Setton LA. Diffusion tensor microscopy of the intervertebral disc anulus fibrosus. Magn Reson Med 1999;41:992–9.
[78] Horton WG. Further observations on the elastic mechanism of the intervertebral disc. J Bone Jt Surg Br 1958;40:552–7.
[79] Natali A, Meroi E. Nonlinear analysis of intervertebral disk under dynamic load. J Biomech Eng 1990;112:358–63.
[80] Ayturk UM, Puttlitz CM. Parametric convergence sensitivity and validation of a finite element model of the human lumbar spine. Comput Methods Biomech Biomed Engin 2011;14:695–705.
[81] Schmidt H, Heuer F, Simon U, et al. Application of a new calibration method for a three-dimensional finite element model of a human lumbar annulus fibrosus. Clin Biomech 2006;21:337–44.
[82] Lee C, Kim Y, Lee C, et al. Impact response of the intervertebral disc in a finite-element model. Spine 2000;25:2431–9.
[83] Wang JL, Parnianpour M, Shirazi-Adl A, et al. Viscoelastic finite-element analysis of a lumbar motion segment in combined compression and sagittal flexion. Effect of loading rate. Spine 2000;25:310–8.
[84] Rohlmann A, Zander T, Bergmann G. Effect of total disc replacement with ProDisc on intersegmental rotation of the lumbar spine. Spine 2005;7:738–43.
[85] Ruberté LM, Natarajan RN, Andersson GB. Influence of single-level lumbar degenerative disc disease on the behavior of the adjacent segments—a finite element model study. J Biomech 2009;42:341–8.
[86] Kiapour A, Ambati D, Hoy RW, et al. Effect of graded facetectomy on biomechanics of Dynesys dynamic stabilization system. Spine 2012;37:E581–9.
[87] Sato K, Kikuchi S, Yonezawa T. In vivo intradiscal pressure measurement in healthy individuals and in patients with ongoing back problems. Spine 1999;24:2468–74.
[88] Suwito W, Keller TS, Basu PK, Weisberger AM, Strauss AM, Spengler DM. New in vivo measurements of pressures in the intervertebral disc in daily life. Spine 1999;24:755–62.
[89] Nachemson A, Morris J. In vivo measurements of intradiscal pressure. J Bone Jt Surg 1964;46:1077–92.
[90] Marchand F, Ahmed AM. Mechanical properties and failure mechanisms of the lumbar disc annulus. Trans Orthop Res Soc 1989;14:355.
[91] Eberlein R, Holzapfel GA, Schulze-Bauer CAJ. An anisotropic model for annulus tissue and enhanced finite element analyses of intact lumbar disc bodies. Comput Methods Biomech Biomed Engin 2001;4:209–29.